

This is an Open Access document downloaded from ORCA, Cardiff University's institutional repository:<https://orca.cardiff.ac.uk/id/eprint/117167/>

This is the author's version of a work that was submitted to / accepted for publication.

Citation for final published version:

Maddalena, Riccardo 2019. Effect of silica particle size on the formation of calcium silicate hydrate using thermal analysis. *Thermochimica Acta* 672 , pp. 142-149.  
[10.1016/j.tca.2018.09.003](https://doi.org/10.1016/j.tca.2018.09.003)

Publishers page: <https://doi.org/10.1016/j.tca.2018.09.003>

Please note:

Changes made as a result of publishing processes such as copy-editing, formatting and page numbers may not be reflected in this version. For the definitive version of this publication, please refer to the published source. You are advised to consult the publisher's version if you wish to cite this paper.

This version is being made available in accordance with publisher policies. See <http://orca.cf.ac.uk/policies.html> for usage policies. Copyright and moral rights for publications made available in ORCA are retained by the copyright holders.



# Accepted Manuscript

Title: Effect of silica particle size on the formation of calcium silicate hydrate using thermal analysis

Author: Riccardo Maddalena Christopher Hall Andrea Hamilton



PII: S0040-6031(18)30732-9

DOI: <https://doi.org/doi:10.1016/j.tca.2018.09.003>

Reference: TCA 78087

To appear in: *Thermochimica Acta*

Received date: 18-9-2017

Revised date: 4-8-2018

Accepted date: 2-9-2018

Please cite this article as: Riccardo Maddalena, Christopher Hall, Andrea Hamilton, Effect of silica particle size on the formation of calcium silicate hydrate using thermal analysis, <![CDATA[*Thermochimica Acta*]> (2018), <https://doi.org/10.1016/j.tca.2018.09.003>

This is a PDF file of an unedited manuscript that has been accepted for publication. As a service to our customers we are providing this early version of the manuscript. The manuscript will undergo copyediting, typesetting, and review of the resulting proof before it is published in its final form. Please note that during the production process errors may be discovered which could affect the content, and all legal disclaimers that apply to the journal pertain.

- C-S-H pastes made with two different silica particle sizes are investigated.
- Isothermal calorimetry is used to study the effect of particle size on the stoichiometry.
- The overall kinetics are well described by a simple exponential (first-order) reaction model

Accepted Manuscript

# Effect of silica particle size on the formation of calcium silicate hydrate using thermal analysis

Riccardo Maddalena<sup>a,c</sup>, Christopher Hall<sup>b</sup>, Andrea Hamilton\*<sup>a</sup>

<sup>a</sup>University of Strathclyde, Department of Civil and Environmental Engineering, Glasgow G1 1XJ, UK

<sup>b</sup>University of Edinburgh, School of Engineering, Edinburgh EH9 3JL, UK

<sup>c</sup>Cardiff University, School of Engineering, Cardiff CF24 3AA, UK

---

## Abstract

Calcium silicate hydrate (C-S-H) is made by mixing calcium hydroxide (portlandite), silica and water at two calcium oxide to silica (C/S) ratios, using nanosilica and silica fume. We investigate how silica particle size influences the rate and extent of formation of C-S-H at room temperature by isothermal calorimetry, thermal analysis, Raman spectroscopy and X-ray diffraction. Rate of reaction increases as silica particle size decreases, and is five times greater with nanosilica than with silica fume. Final composition depends only on initial C/S ratio. Compositions at 28 days are estimated from thermogravimetric and X-ray diffraction data. There is a weak maximum in the reaction rate of nanosilica pastes about 20–30h after mixing. The overall kinetics are well described by a simple exponential (first-order) reaction model. The early-time reaction rate around the rate maximum is described by an Avrami model.

*Keywords:* calcium silicate hydrate, nano-silica, silica fume, heat of hydration, calorimetry, Raman spectra

---

## <sup>1</sup> 1. Introduction

<sup>2</sup> Increasing awareness of climate change and greenhouse gas emissions has  
<sup>3</sup> led researchers to develop alternative materials to control the environmental  
<sup>4</sup> impact of manufacturing industries. Cement production is responsible for about  
<sup>5</sup> 7–10% of the total anthropogenic CO<sub>2</sub> emissions [1]. In recent years cement

has been partially replaced by the addition of waste by-products such as fly ash and amorphous silica [2, 3, 4, 1, 5]. Fly ash is well established in the cement industry as an environmentally friendly replacement for cement at up to 35 wt% [6], without compromising the mechanical and physical properties of concrete [7]. Amorphous forms of silica, such as silica fume and nano-silica, have also been investigated. Silica fume is a by-product of the silicon and ferro-silicon industry, with a nominal particle size range of 100–1000 nm, while commercial nano-silica is *ad-hoc* synthesised from sodium silicate using a sol-gel technique. Recent investigations have also explored the production of ‘green’ nano-silica from waste dunite, which has a comparatively lower environmental footprint [8]. Silica fume has been shown to enhance the mechanical strength of Portland cement, reduce permeability and thermal conductivity [9, 10, 1], and accelerate the early hydration of C<sub>2</sub>S, C<sub>3</sub>A and C<sub>4</sub>AF [11], while nano-silica enhances strength from increased production of additional C-S-H [4]. (Here we use the standard abbreviations C = CaO, S = SiO<sub>2</sub>, H = H<sub>2</sub>O generally employed in cement chemistry). The smaller particle size of nano-silica produces a correspondingly greater surface area to provide nucleation sites for the growth of C-S-H [12, 13].

Thermal analytical techniques are extremely useful not only in understanding the hydration kinetics of cement, but also in providing reaction models to tailor cement paste for specific applications. Kumar *et al.* [14] studied the effect of fly ash on the hydration of ordinary Portland cement by isothermal calorimetry and found that while the addition of 20 wt% fly ash retards the hydration, this effect is negated by addition of 5 wt% of calcium hydroxide. Wei *et al.* [11] used TG/DSC to study hydrated cement modified by silica fume. They found that silica fume accelerates the early hydration of cement and stabilizes ettringite, and therefore reduces damage to the set cement and concrete from delayed ettringite formation. However, when silica-fume is combined with fly ash, the overall effect is a delayed hydration [15]. Oltulu and Sahin (2014) [16] studied the pore-structure development of cement mortars containing silica fume and other nano-powders. The addition of nano-silica resulted in an increased

amount of C-S-H and other hydrated products. On the other hand, it has been shown that an increasing content of silica fume in Portland cement results in a lower C/S ratio of the C-S-H [17]. Thermogravimetric analysis and calorimetry data have been used to determine the pozzolanic reaction of supplementary cementitious materials (such as fly ash) and to describe the cement or concrete hydration reaction, and validated results were useful in establishing models for the hydration of cement [18, 19]. Although there are several experimental reports of the beneficial effects of amorphous silica added to cement, little research has been conducted on the effect of silica particle size on the formation of the C-S-H phases responsible for early strength and hardening [20]. This is partly due to the difficulty of accurately quantifying the C-S-H content when it is found among other hydrated products such as ettringite and the calcium aluminate hydrates [20]. Nonetheless, the C-S-H formed in cement by hydration of alite ( $C_3S$ ) and belite ( $C_2S$ ) or in cement-alkali systems is morphologically different from synthetic C-S-H. In the first case C-S-H assumes the typical fibrillar habit, whereas in synthetic formation it tends to form with a two-dimensional ‘crumpled foil’ habit which, according to Richardson [21, 22], indicates that the C-S-H has less space constraint during growth. A clearer understanding of C-S-H behaviour is obtained by isolating it from other accessory minerals, while the behaviour of pure C-S-H (made without the hydration of Portland cement clinker) is of significant relevance to the fields of nuclear waste and environmental contaminant trapping as C-S-H is the component which adsorbs.

59

In this work we prepared C-S-H in isolation from other mineral phases, and studied its formation by thermal analysis and isothermal calorimetry, supported by Raman spectroscopy and X-ray diffraction. We synthesised C-S-H by reacting calcium hydroxide with silica and varying the calcium to silica (C/S) ratios. The effect of the silica particle size on the formation of C-S-H was investigated using two different silica sources: silica fume (particle size range 100–1000 nm) and nano-silica (particle size range 5–20 nm). We show how silica particle size and hydration kinetics affect the extent of reaction at 28 days and the final

68 composition.

69

70 **2. Materials and methods**

71 *2.1. Materials*

72 C-S-H phases were synthesised using reagent grade calcium hydroxide (port-  
 73 landite) powder (Sigma Aldrich, CAS number 1305-62-0), aqueous-suspension  
 74 nano-silica (Sigma Aldrich Ludox T50 nano-SiO<sub>2</sub>, CAS number 7631-86-9), and  
 75 silica fume SF920D (Elkem Microsilica, Norway, CAS number 69012-64-2). To  
 76 minimise carbonation during mixing, deionised and decarbonated water was  
 77 used [23]. Physicochemical properties of the starting materials are reported in  
 78 Table 1. X-ray patterns (Figure 1) show that the silica fume and nano-silica  
 particles used are essentially amorphous.

Table 1: Properties of calcium hydroxide (CH), nano-silica suspension Ludox T50 (NS), and silica fume SF920D (SF)

Material	Calcium hydroxide	Nano-silica (NS)	Silica fume (SF)
Form	Dry powder	Suspension in H <sub>2</sub> O	Dry powder
Assay	Ca(OH) <sub>2</sub> : ≥ 95.0% Reagent grade	SiO <sub>2</sub> : 50.0%	SiO <sub>2</sub> : ≥ 90.0%
	CaCO <sub>3</sub> : ≤ 3.0		
Anion traces	Cl <sup>-</sup> : ≤ 0.03%	Cl <sup>-</sup> : ≤ 0.05%	
Cation traces	Na, K, Mg ≤ 0.05%		
pH at 25 °C	12.4 (slurry)	8.5–9.5	–
Particle size range (nm)	–	5–20	100–1000
Density at 25 °C (g cm <sup>-3</sup> )	2.24	1.40	2.2–2.3
Specific area (m <sup>2</sup> g <sup>-1</sup> )	20–41 (hydrated)	110–150	15–30

79

80 C-S-H pastes were mixed manually in a nitrogen environment at room tem-  
 81 perature. Calcium hydroxide, silica (either silica fume or nano-silica) and water  
 82 were mixed at a liquid:solid weight ratio of 2.0. Two different target lime (CaO)  
 83 to silica (C/S) ratios, 0.81 and 2.4 mol/mol, were investigated (Table 2). These

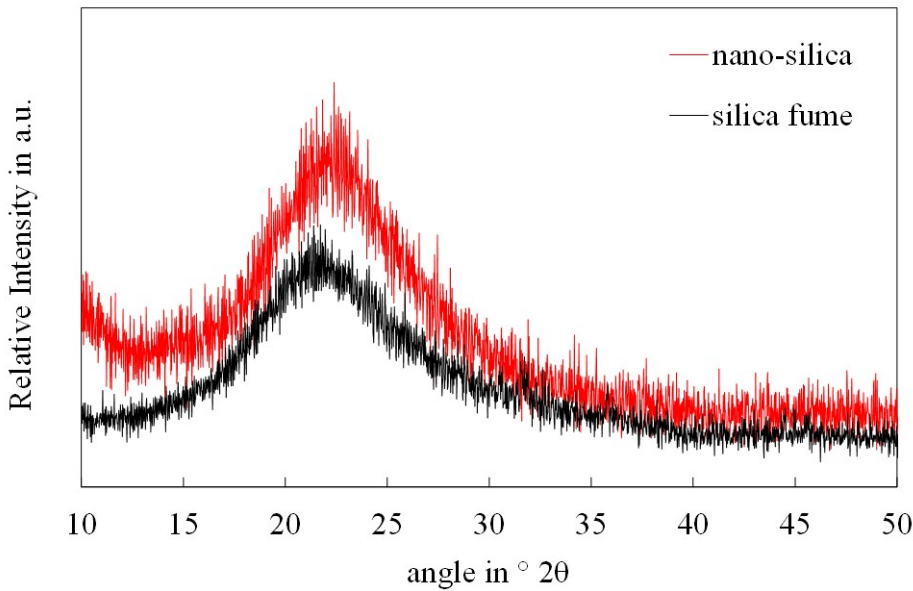


Figure 1: X-ray diffraction patterns of amorphous silica fume and nano-silica, showing broad diffuse scattering.

84 mol ratios correspond to the ratios 1:1 and 3:1 portlandite:silica by weight.  
 85 Specimens were cast in cube moulds, stored in a sealed environment at 20 °C,  
 86 100% RH, and cured for 28 days. After curing, the samples were demoulded,  
 87 immersed in an acetone bath for 24 h to arrest the hydration process [24, 25],  
 88 and then placed in a drying chamber under a nitrogen flow. All samples were  
 89 then ground by hand and sieved to obtain a homogeneous fine powder, and  
 90 stored in a sealed environment.

91

## 92 2.2. Materials characterisation and thermal analysis

93 Powder XRD analyses were performed using a Bruker D8 Advance diffractometer with CuK $\alpha$  radiation over the range 10–60° 2 $\theta$ , step size of 0.02° and  
 94 scan rate of 0.5 s/step. The samples were also characterised by Raman spectroscopy, using a Renishaw InVia spectrometer equipped with Modulaser Stellar Pro ML/150 argon ion laser (785 nm). Raman shifts were recorded over a

Table 2: Sample mixes, silica source (silica fume, SF or nano-silica, NS), and initial mix and paste compositions

Mix ID	Silica source	Initial mix composition			
		CH/S by wt	C/S mol/mol	CH g/g paste	S
SF24	SF	3:1	2.4	0.25	0.083
SF081	SF	1:1	0.81	0.167	0.167
NS24	NS	3:1	2.4	0.25	0.083
NS081	NS	1:1	0.81	0.167	0.167

98 9 point map ( $200 \times 200 \mu\text{m}$ ) and wave-number range of 100–4000  $\text{cm}^{-1}$ , us-  
 99 ing the  $\times 20$  objective lens. The exposure time was 10 s, and each spectrum  
 100 was accumulated three times. Peaks were fitted to a gaussian lineshape us-  
 101 ing PeakFit (T.C. O’Haver) in Matlab. Specific heat flow and heat of reaction  
 102 were measured using an isothermal calorimeter (I-Cal 4000 HPC, Calmetrix).  
 103 Fresh paste (about 40 g) was cast into a cylindrical container and placed into  
 104 the calibrated calorimeter, at a constant temperature of  $21 \pm 2^\circ\text{C}$ . The heat  
 105 flow was recorded over 200 h. Samples were mixed externally, hence the first  
 106 5–10 min of detected heat flow were not taken into account for further calcu-  
 107 lations. Thermo-gravimetric (TG) and differential scanning calorimetry (DSC)  
 108 data were collected using a NETSCH STA 449 F1 Jupiter instrument. Mea-  
 109 surements were made on 10–20 mg powder samples, under constant nitrogen flow  
 110 at a heating rate of  $10^\circ\text{C min}^{-1}$  from  $25^\circ\text{C}$  to  $1000^\circ\text{C}$ . Results are plotted  
 111 as weight loss (%) and heat flow ( $\text{mW mg}^{-1}$ ) as a function of the temperature  
 112 ( $^\circ\text{C}$ ). TG measurement results were also used to calculate the final C/S molar  
 113 ratio of the samples, according to the methodology of Garbev *et al.* [26].  
 114

<sup>115</sup> **3. Results and discussions**

<sup>116</sup> *3.1. XRD characterisation and Raman spectroscopy*

<sup>117</sup> XRD patterns were obtained on specimens of all four mixes at 28 d (Fig 2).

These were intended primarily to provide information on mineralogy and struc-

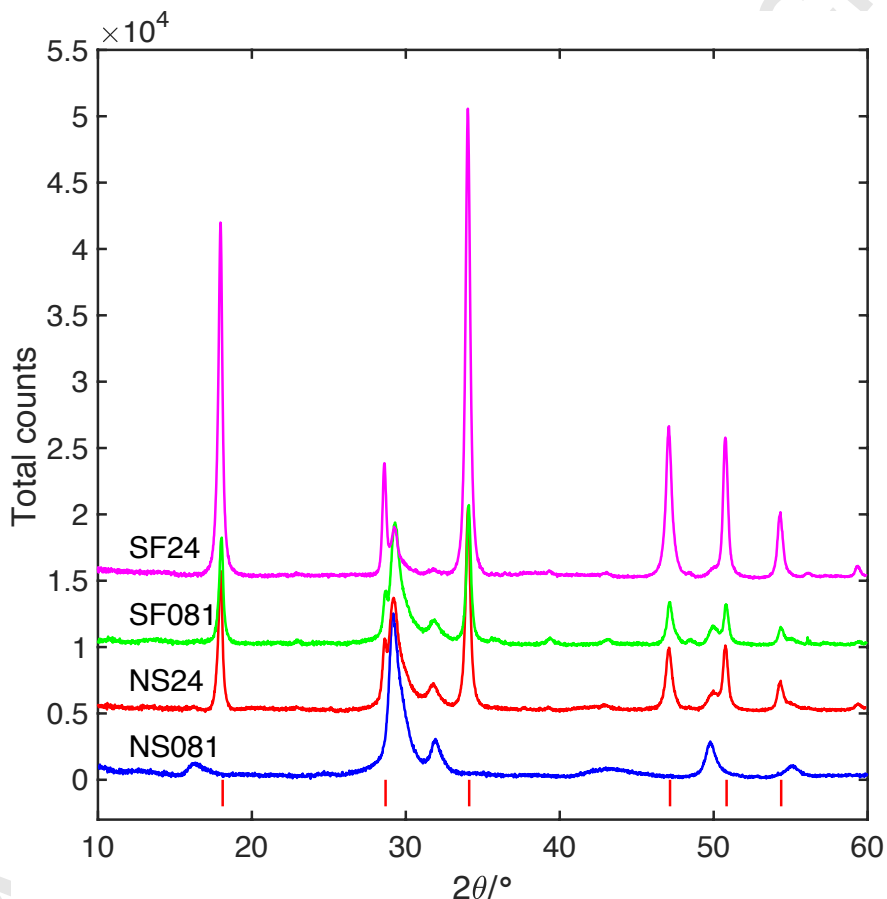


Figure 2: XRD patterns of dried solid material from all mixes after 28 d reaction. Small zero corrections have been applied to the  $2\theta$  scale to align peak positions. The principal diffraction lines of portlandite are shown as red ticks.

<sup>118</sup>

<sup>119</sup> ture, but quantitative peak-area analysis also provides support for the TGA  
<sup>120</sup> composition results. The XRD patterns show the main features expected of

<sup>121</sup> C-S-H(I) [26, 27, 28, 29], namely a strong reflection at  $\sim 29.3^\circ$   $2\theta$ , and other  
<sup>122</sup> prominent reflections at  $\sim 34.1^\circ$ ,  $\sim 49.7^\circ$ . These correspond to the (020), (200)  
<sup>123</sup> and (240) reflections of tobermorite [27]. The (002) basal reflection at  $\sim 6.6^\circ$   
<sup>124</sup> was outside the scan range and was not observed.

<sup>125</sup> In NS24, SF081 and SF24, portlandite was present, with principal peaks at  
<sup>126</sup> the positions shown in Fig 2. In NS081, all of the portlandite in the original  
<sup>127</sup> mix has been consumed, and we have an uncontaminated C-S-H pattern of  
<sup>128</sup> low C/S ratio. We note that in all patterns the strong (020) peak at  $29.3^\circ$  is  
<sup>129</sup> markedly asymmetric. The weak (101) reflection at  $\sim 16.1^\circ$   $2\theta$  is visible only  
<sup>130</sup> in the low C/S mixes NS081 and SF081, an observation consistent with the  
<sup>131</sup> comment of Tajuelo Rodriguez *et al.* [28] who find that this peak decreases in  
<sup>132</sup> intensity as the C/S ratio increases. Likewise the broad reflection at  $\sim 44^\circ$  is  
<sup>133</sup> visible only in the NS081 pattern. A comparison of pseudo-Voigt peak areas  
<sup>134</sup> allows us to estimate approximate compositions from the XRD patterns, using  
<sup>135</sup> the NS081 pattern which contains no portlandite as a C-S-H reference. The  
<sup>136</sup> estimated compositions from XRD are in good agreement with those from TGA  
<sup>137</sup> (Table 6).

<sup>138</sup> The Raman spectra of the samples are reported in Figure 3 with peak po-  
<sup>139</sup> sitions given in Table 3. The first low frequency bands in the range 200–  
<sup>140</sup>  $305\text{ cm}^{-1}$  correspond to the Ca-O lattice vibrations in calcium carbonate. As  
<sup>141</sup> demonstrated by Black *et al.* [30], these bands are only visible in samples which  
<sup>142</sup> have begun to carbonate through exposure to air and are not present in fresh  
<sup>143</sup> paste sealed from the environment. One is weakly present in NS081 at  $279\text{ cm}^{-1}$   
<sup>144</sup> but it is poorly resolved compared to the bands at 270 and  $302\text{ cm}^{-1}$  shown  
<sup>145</sup> by Black *et al.* and our assignment is tentative. Carbonation is more obvi-  
<sup>146</sup> ously demonstrated in NS24, the sample with the highest C/S ratio and which  
<sup>147</sup> contains 41 wt.% portlandite by the doublet at 1075 and  $1085\text{ cm}^{-1}$ . Black  
<sup>148</sup> *et al.* attribute this to the  $\nu_1[\text{CO}_3]$  mode but it is significantly weaker than  
<sup>149</sup> the very strong bands they find in samples exposed for 1 month. We conclude  
<sup>150</sup> that our samples are lightly carbonated which fits with our sample preparation  
<sup>151</sup> procedure. The presence of portlandite is clear from the intense peaks at c. 355

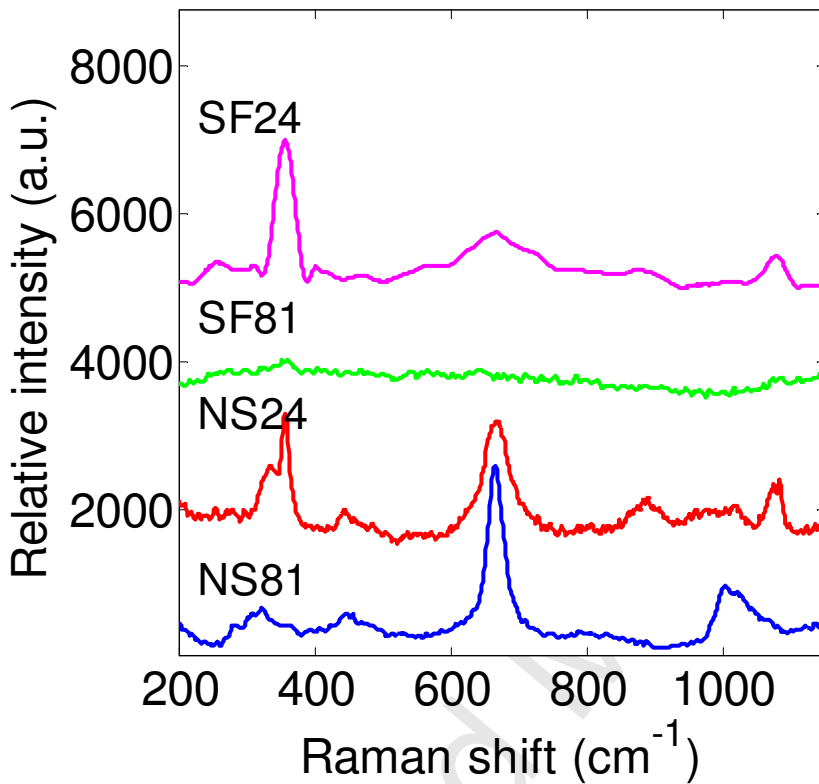


Figure 3: Raman spectra

<sup>152</sup>  $\text{cm}^{-1}$  in the spectra for samples NS24 and SF24, which are assigned to  $\text{Ca}(\text{OH})_2$   
<sup>153</sup> external translation mode,  $A_{1g}$  showing that the samples have not significantly  
<sup>154</sup> carbonated as these bands are barely present after 40 hours of exposure in the  
<sup>155</sup> carbonation study by Black *et al.* Ca-O lattice vibrations from C-S-H gel are  
<sup>156</sup> described as occurring at 319–333  $\text{cm}^{-1}$  in fresh samples of C/S ratio 0.5–1.5 [31]  
<sup>157</sup> which broaden and move to lower frequencies upon carbonation, possibly due  
<sup>158</sup> to weakening of the Ca-O bonds during C-S-H decalcification [30]. We see the  
<sup>159</sup> band increase in frequency from 316–332  $\text{cm}^{-1}$  as the C/S ratio increases from  
<sup>160</sup> 0.79 (NS081) to 1.70 (NS24) which is in line with Garbev *et al.* The band at  
<sup>161</sup> 445  $\text{cm}^{-1}$ , attributed to O-Si-O bending vibrations in  $\text{SiO}_4$  where the oxygen

Table 3: Position of the Raman peaks ( $\text{cm}^{-1}$ ) for samples NS081, NS24 and SF24

NS081	NS24	SF24	Assignment
279 (w)	–	252	lattice vibrations, Ca-O in $\text{CaCO}_3$
316, 360 (w)	332	–	lattice vibrations, Ca-O in C-S-H
–	356 (vs)	354 (vs)	$\text{A}_{1g}$ external translation mode in $\text{Ca(OH)}_2$
446 (w)	447 (w)	–	$\text{SiO}_4$ mainly O(non)-Si-O(non) bending
665 (vs)	666 (s)	663	symmetric bending Si-O-Si, C-S-H
~770–900	885	885	$\text{SiO}_4$ symmetric stretch of $\text{Q}^1$
~1004	1018	1013	$\text{SiO}_4$ symmetric stretch of $\text{Q}^2$
–	1075, 1085	1079	$\text{CO}_3$ symmetric stretch

w: weak, s: strong, vs: very strong.

is non-bridging is present at 446 and 447  $\text{cm}^{-1}$  in this work and is relatively weak, as shown in Figure 3. The strongest peak present in our spectra at 666  $\text{cm}^{-1}$  is produced by Si-O-Si symmetric bending vibrations in C-S-H which have been shown to broaden with increasing C/S ratio from the presence of silicate dimers [31]. This effect can be seen in Figure 3 as the peak width increases (FWHM) from 28 (NS081, C/S=0.79) to 35 (NS24, C/S=1.70). A very weak peak at  $\sim 885 \text{ cm}^{-1}$  is visible in the higher C/S ratio samples (NS24 and SF24), which is assigned to the symmetric stretch of  $\text{SiO}_4$  dimers ( $\text{Q}^1$ ) by Garbev *et al.* who show it increases in intensity with increasing C/S ratio and is barely visible when the C/S ratio is less than 0.83. The peak at  $\sim 1004 \text{ cm}^{-1}$  in Figure 3 is strongest but also broadest in the spectra for NS081. The position is determined manually as the peak has a long asymmetric tail after the apex. This band is assigned to the symmetric stretch of  $\text{SiO}_4$  chains ( $\text{Q}^2$ ) and is described by Garbev *et al.* [31] as increasing in frequency with C/S ratio to a final value of 1022  $\text{cm}^{-1}$  in samples with C/S 1.33 and 1.55. We see an increase in frequency from c. 1004  $\text{cm}^{-1}$  at C/S = 0.79 to 1018  $\text{cm}^{-1}$  at C/S = 1.70. The significant asymmetry of the peak in NS081 can be attributed to disorder in the silicate polymerisation and presence of different silicate species, such as long chains,

180 octamers and pentamers [31]. The weak and comparatively narrow bands in  
 181 NS24 and SF24 suggests only a few, uniform, Q<sup>2</sup> species are present [31]. As  
 182 already discussed, CO<sub>3</sub> symmetric stretch ( $\nu_1$ ) modes occur at  $\sim$ 1080 cm<sup>-1</sup>  
 183 and are more clearly present in the samples with significant portlandite (SF24  
 184 and NS24) but are still weak by comparison with spectra from the 1 month old  
 185 samples described by Black [30]. By comparison with NS spectra, the SF spec-  
 186 tra, in particular SF81 are surprisingly featureless. Overall, the Raman spectra  
 187 confirms the XRD and TGA evidence that there is only slight carbonation in  
 188 the samples.

189 *3.2. Isothermal calorimetry*

The calorimetric heat flow rate (Figure 4) shows the following features:

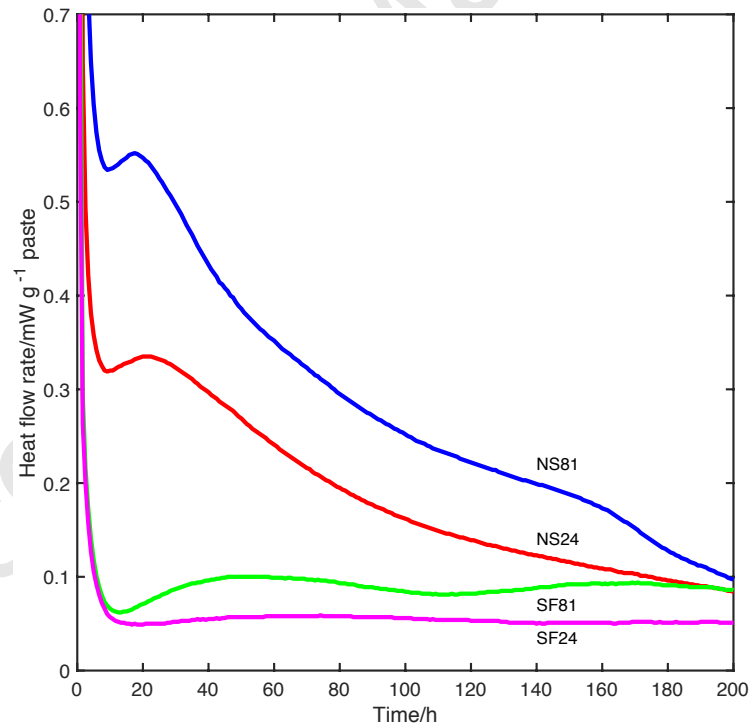


Figure 4: Heat flow rate for all mixes measured by isothermal calorimetry over a reaction time of 0–200 h.

190

- 191        1. An initial period of a few minutes in which the heat flow rate is high  
 192              but falls rapidly; the heat evolved over this short initial period no doubt  
 193              includes contributions from wetting and dissolution as well as early-time  
 194              reaction, and also non-isothermal effects in the calorimeter.
- 195        2. A period of some hours in which the heat flow rate slowly decreases until  
 196              a minimum is reached (the slow-rate or decelerating rate period).
- 197        3. After the minimum, the heat flow rate increases (the accelerating rate  
 198              period) for some hours until it reaches a maximum.
- 199        4. Beyond the maximum, the heat-flow rate decreases slowly but in all cases  
 200              is still measurable at 200 h.

201        We follow the usual practice of treating the calorimetric heat-flow rate after  
 202        the initial period as a direct measure of the rate of formation of C-S-H. The  
 203        features we identify are similar in several ways to those observed in calorimetric  
 204        data for the hydration of tricalcium silicate C<sub>3</sub>S [32, 20, 33, 34]. As here, C<sub>3</sub>S  
 205        hydration also shows a so-called slow-reaction period, followed by an accelerating  
 206        period, which in turn is followed by a final extended period of decreasing heat  
 207        flow rate. On the other hand, although the early-time minimum and maximum  
 208        in the reaction rate are well defined, at least in the nano-silica systems, they are  
 209        much less prominent than in C<sub>3</sub>S hydration where the minimum heat-flow rate  
 210        is close to zero [33]. Apart from these small variations in the hydration rate at  
 211        early times, we find the overall hydration kinetics are accurately described by  
 212        a simple exponential model. This is readily seen by considering the cumulative  
 213        heat evolved (the area under the heat flow rate curve), which we can fit to the  
 214        equation

$$H = b + H_0[1 - \exp(-kt)] \quad (1)$$

215        where  $H(t)$  is the cumulative heat evolved at time  $t$ ,  $H_0$  is the heat of reaction,  
 216         $k$  is a rate constant, and  $b$  is a constant to take account of initial heat-flow spike.  
 217        Equation 1 is the standard first-order model of solid-state reaction kinetics [35].  
 218        Figure 5 shows that using data from about 50 h onwards allows us to extract  
 219        values of rate constant  $k$  and heat of reaction  $H_0$  for the four mixes. The

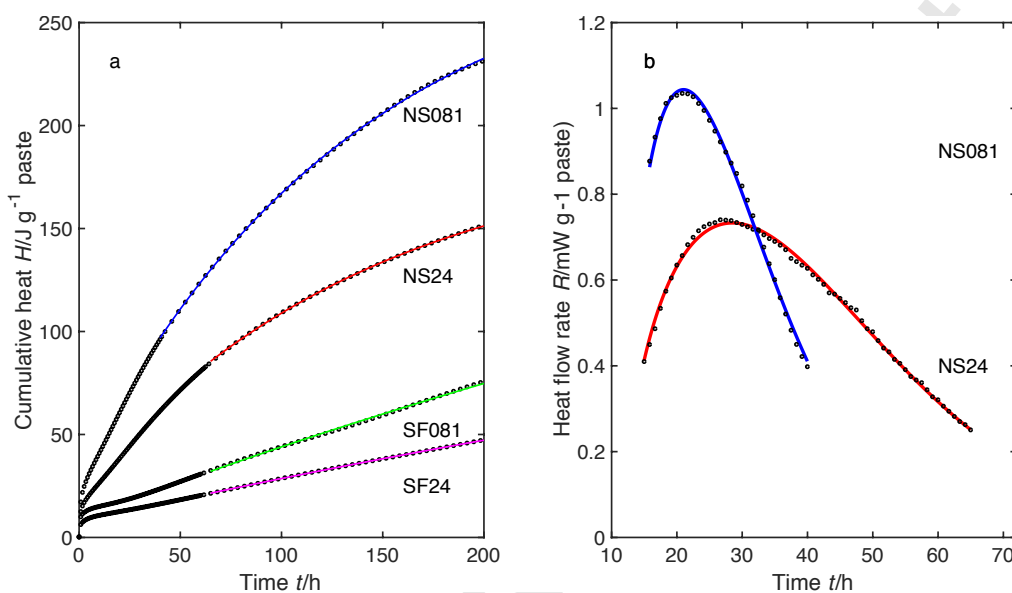


Figure 5: (a) Cumulative heat release  $H$  in the first 200 h of reaction, showing least-squares fits to Equation 1. (b) Heat flow rate  $R$  for nano-silica mixes NS81 and NS24, showing least-squares fits to Equation 3.

parameter values are given in Table 4.

The effect of particle size is clear from our (admittedly limited) data. The rate of hydration is much faster in the NS mixes than in the SF mixes, with  $k$  values being about five times smaller. This is approximately the same as the ratio of the specific surface areas (see Table 1), which is  $\sim 5.8$ . The duration of the reaction can be estimated as  $\tau = 4.61/k$ , at which time the reaction is 99% complete. This shows that the NS mixes have fully reacted at 28 days. The SF mixes have only reached  $\sim 60\%$  of their final composition at 28 days, and take 4–5 months to reach 99 % completion. The parameter  $H_0$  is also informative. The NS81 and SF81 mixes have the same silica content per unit weight of paste (Table 4), and we see that the ultimate heat of reaction which is the same for both does not depend on particle size. Likewise for the NS24 and SF24 systems.

Table 4: Parameters of least-squares model fit to Equation 1

Mix ID	Fit parameters, Equation 1				
	$k$ $\text{h}^{-1}$	$H_0$ J per g paste	$H_0$ kJ/g SiO <sub>2</sub>	$H_0$ kJ/mol SiO <sub>2</sub>	$b$ J per g paste
NS81	0.0074	263	1.58	94.7	29.4
NS24	0.0070	169	2.03	122.2	23.7
SF81	0.0014	(265)	1.59	95.5	8.5
SF24	0.0013	173	2.08	125.0	7.4

232 On the other hand, the NS81 mix contains exactly twice as much silica per unit  
 233 weight of paste as the NS24 mix (see Table 4), but  $H_0$  (per g of paste) of NS81  
 234 is significantly less than twice that of the NS24 mix. The observed ratio is 1.51.  
 235 This suggests that there is unreacted residual silica in the NS81 systems, and  
 236 that the true C/S ratio is greater than the nominal (molar) target value of 0.81.  
 237 The same comparison can be made between the SF81 and SF24 mixes, with the  
 238 same conclusion. Expressed per mol SiO<sub>2</sub>,  $H_0$  is essentially the heat of reaction,  
 239 which is smaller for the NS81 and SF81 mixes than for the NS24 and SF24  
 240 mixes. Once again, this allows the possibility that the NS81 and SF81 mixes  
 241 contain unreacted silica at the end of the reaction, and that the true C/S ratio  
 242 of the C-S-H formed is greater than the nominal value. The heats of reaction are  
 243 comparable with those reported for other C-S-H forming systems, but further  
 244 thermodynamic analysis is outside the scope of this study.

245 *3.2.1. Early-time behaviour and the rate maximum*

246 The similarities between the hydration of the silica/portlandite system de-  
 247 scribed here and that of the C<sub>3</sub>S system are noteworthy. The same maximum  
 248 in reaction rate can be seen in the calorimetric data on nano-silica/portlandite  
 249 systems reported by Lin *et al.* [36], although it is not discussed. The existence of  
 250 an early slow-reaction period is generally regarded as a particular feature of the  
 251 hydration of calcium silicate systems. Yet it is observed here in a system where

the Ca concentration in solution is buffered by the presence of excess solid portlandite, and where the C-S-H can only form by transport of Ca through solution to the silica surface. This is in sharp contrast to the case of C<sub>3</sub>S hydration where both Ca and Si are co-located, and only water is required for reaction; furthermore, because the C/S ratio of the C-S-H product is <3, there must be a net outward diffusion of Ca into solution, rather than an inward transport as here. In the C<sub>3</sub>S case, the accelerating-rate period following the minimum is generally described by means of a nucleation and growth [NG] mechanism, often using the Avrami or Cahn models, or variants. NG models ascribe the hydration kinetics to the interplay of nucleation rates and crystal-growth rates, and assume that simple diffusive transport is not rate-controlling. It is however recognised that at long times the reaction rate is likely to be controlled by diffusion of reactant species through the C-S-H to the unhydrated surface beneath. Thus the long tail in the C<sub>3</sub>S heat-flow rate at extended times is not represented by NG models. We find that the early-time heat flow data for the nano-silica mixes NS81 and NS24 can be represented by a simple stretched-exponential Avrami model for the extent of reaction  $X$  at time  $t$

$$X = 1 - \exp(-k_2 t^m) \quad (2)$$

where  $k_2$  is a rate constant, and  $m$  is a constant. The heat flow rate  $R$  is proportional to  $dX/dt$ , so that for this model

$$R = amk_2^m(t - t_0)^{m-1} \exp[-[k_2(t - t_0)]^m] \quad (3)$$

where  $t_0$  is a time-offset and  $a$  is a constant. We show results in Fig 5b, with fit parameters given in Table 5. In the data analysis, we have calculated the difference between the measured cumulative heat flow and the simple exponential model, and differentiated this numerically to obtain the non-exponential contribution. That we can fit the data with such a model does not have any clear mechanistic implications, but the existence of the rate minimum and maximum is unexpected, and future work may provide an explanation. The values of the constant  $m$  are rather lower than the typical Avrami values of 2–3. We note

Table 5: Parameters of model fit to Equation 2

Mix ID	Fit parameters, Equation 3		
	$k_2$	$m$	$a$
	$\text{h}^{-1}$	–	$\text{mW per g paste}$
NS81	0.054	1.50	26.1
NS24	0.030	1.52	32.7

Time-offset  $t_0 = 12 \text{ h}$

<sup>279</sup> that of course the Avrami model (in its site-saturation form) reduces to our  
<sup>280</sup> simple exponential form when  $m = 1$ .

<sup>281</sup> *3.3. Thermal analysis*

<sup>282</sup> TG/DSC curves of C-S-H samples hydrated for 28 days are shown in Figure  
<sup>283</sup> 6. Thermogravimetric curves are typical of C-S-H with a total weight loss of 30–  
<sup>284</sup> 35%. The first thermal step is observed in the range 25–200 °C and corresponds  
<sup>285</sup> to the evaporation of pore and capillary water and dehydration of C-S-H [26, 4].  
<sup>286</sup> The second weight loss occurs between 350–550 °C and is associated with the  
<sup>287</sup> dehydroxylation of portlandite. The thermal step in the range 600–700 °C  
<sup>288</sup> is attributed to the loss of CO<sub>2</sub> from calcium carbonate, due to the surface  
<sup>289</sup> carbonation of samples during instrument operations [26]. As noted in [28], there  
<sup>290</sup> is a small continuous weight loss over much of the temperature range, and this  
<sup>291</sup> is attributed to continuing dehydration of C-S-H. TG results are summarised  
<sup>292</sup> in Table 6. The weight loss values for portlandite and calcite were found by  
<sup>293</sup> a simple tangent method [37]. The weight loss was obtained as difference in  
<sup>294</sup> weight at the intersections of the tangent drawn at the point of maximum slope  
<sup>295</sup> in the weight loss curve and straight lines fitted to the data above and below  
<sup>296</sup> the decomposition.

<sup>297</sup> At 28 days, samples made with nano-silica contain more C-S-H than samples  
<sup>298</sup> made with silica fume. In agreement with Raman and XRD analysis, at the  
<sup>299</sup> same initial stoichiometric C/S ratio, nano-silica promotes the formation of C-

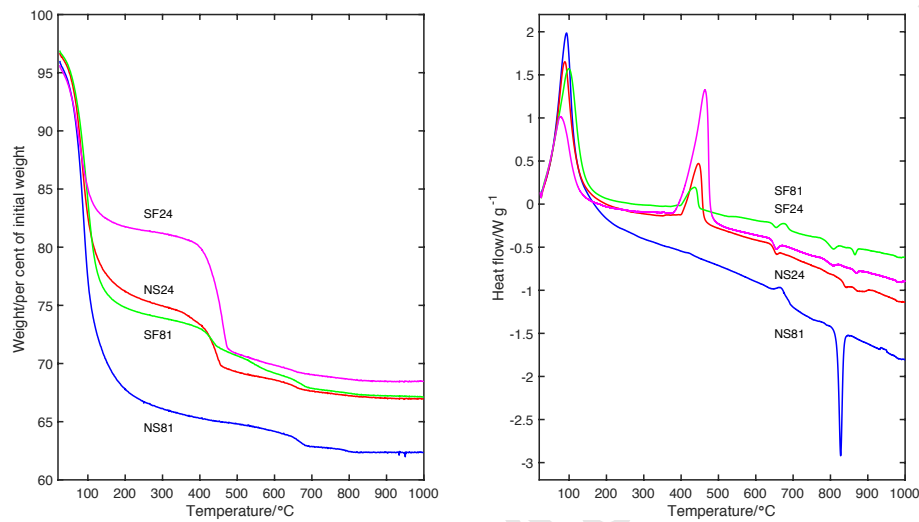


Figure 6: TG and DSC curves of all samples. Left: Thermogravimetric data; right: DSC response, exothermic reaction as downward deflection.

300 S-H and no  $\text{Ca}(\text{OH})_2$  is detected in the mix NS81. Additionally, the portlandite  
 301 content, proportional to the weight loss, in %, in the range 350–550 °C, is  
 302 higher in samples made with silica-fume, where it is up to 40 wt%. TG data  
 303 were used to calculate the C/S ratio of hydrated samples (final C/S ratio at  
 304 28 days of hydration), according to the methodology described in Garbev *et al.*  
 305 [38]. Results are reported in Table 7. Using nano-silica instead of silica fume  
 306 as the silica source, results in an overall higher final C/S ratio. This reflects  
 307 the higher reactivity of nano-silica and its capability to form additional C-S-  
 308 H. The calculated C/S ratio values should be taken more as a guide rather  
 309 than absolute. In sample NS081, while the reaction went to completion at 28d,  
 310 the calorimetry data suggests some unreacted silica, which indicates the C/S  
 311 ratio is higher than the nominal value. Sample NS24, the reaction was also  
 312 complete by 28 days and the system had an excess of calcium, expressed as  
 313 wt% portlandite, so it is unlikely there is any unreacted silica. The C/S value

Table 6: Composition of reacted mixes at 28 d: TG and XRD results

Mix ID	Fraction of total CaO as				
	C-S-H		Portlandite		Calcite
	TGA	XRD	TGA	XRD	TGA
NS81	0.980	1.0	0	0	0.02
NS24	0.597	0.62	0.396	0.38	0.008
SF81	0.792	0.83	0.193	0.17	0.016
SF24	0.302	0.30	0.695	0.70	0.003

Notes: Calcite was not determined by XRD analysis

<sup>314</sup> of 1.7 is higher than anticipated from a synthetic C-S-H, where an upper value of  
<sup>315</sup> 1.6 [39] is expected, this could be explained by the slow decomposition of some  
<sup>316</sup> nano-crystalline portlandite trapped within the C-S-H pores. Calorimetry data  
<sup>317</sup> shows that at 28 days, both silica fume samples had not finished reacting and  
<sup>318</sup> therefore the C/S ratio is likely to be higher than calculated due to unreacted  
<sup>319</sup> silica.

Table 7: Mix compositions at 28 d and calculated initial (nominal) and measured C/S molar ratios, from thermogravimetric analysis

Mix ID	Portlandite	Calcite	C/S	
			initial	final
			wt%	mol ratio
NS81	0	1.3	0.81	0.79
NS24	19.3	0.65	2.4	1.70
SF81	7.3	0.88	0.81	0.66
SF24	39.5	0.22	2.4	1.02

Note: Decomposition temperature ranges: portlandite, NS24 338–495 °C,  
SF81 338–460 °C, SF24 338–500 °C; calcite, 630–690 °C, except NS24  
625–690 °C.

320 The C/S ratio plays a key role in the hydration kinetics of Portland cement  
321 and its strength development [40]. In hydrated Portland cement, it varies in  
322 the range 0.6–2.0 mol/mol, and many authors have found that mortar and  
323 concrete pastes modified by the addition of pozzolanic nano-particles produce  
324 a denser C-S-H with a lower C/S ratio [41, 42, 43]. Results presented here  
325 show that at 28 days, which is the standard curing time for most applications,  
326 the C/S ratio is increased by smaller particles. This is due to the enhanced  
327 reactivity of nano-silica compared to that of silica fume. C/S ratio is a key  
328 parameter for specific application and not only in cement industry: C-S-H can  
329 be crystallographically tailored to incorporate radionuclides or heavy metals into  
330 its structure [44, 45], or could be expanded to increase porosity and be used in  
331 waste-water treatment as an adsorbent material [46, 47]. Hence, understanding  
332 the effect of fine additives on the C/S ratio and quantity is valuable.

333 Results of the differential scanning calorimetry of samples hydrated for 28  
334 days (curves shown in Figure 6) are summarised in Table 8. DSC curves show  
335 the first endothermic event at about 80 °C, corresponding to the formation of  
336 C-S-H and evaporation of pore water. The integrated peak area is greater in  
337 sample NS081 ( $603 \text{ J g}^{-1}$ ) than sample SF081 ( $586 \text{ J g}^{-1}$ ). Correspondingly,  
338 the endothermic event at about 430 °C, associated with the decomposition of  
339  $\text{Ca(OH)}_2$ , is greater in samples with higher nominal C/S ratio and/or larger  
340 silica particle size range (sample NS24,  $195 \text{ J g}^{-1}$ ; sample SF24,  $533 \text{ J g}^{-1}$ ).  
341 Furthermore, the higher C/S ratio causes a shift of the DSC peak, which rep-  
342 resents portlandite breakdown, towards a higher temperature, and close to the  
343 peak centre of pure portlandite, at 460 °C. The DSC response of sample NS081  
344 exhibits a narrow exothermic peak at around 800 °C, attributed to the crys-  
345 tallisation of wollastonite [48, 49, 44, 28].

346 **4. Conclusions**

347 We report the results of a study of the formation of C-S-H by reaction  
348 of amorphous silica and portlandite at low and high C/S ratio (0.81 and 2.4

Table 8: DSC peak information: peak height, centre and integrated area in the decomposition range of C-S-H (25–200 °C) and portlandite (350–550 °C)

Mix ID	C-S-H 25–200 °C			Portlandite 350–550 °C		
	centre °C	height mW/mg	area J/g	centre °C	height mW/mg	area J/g
SF81	99	1.58	586	436	0.19	66.4
SF24	78	1.02	320	464	1.32	533
NS81	93	1.99	603	—	—	—
NS24	88	1.65	496	446	0.47	195

Note: NS81, no portlandite detected

349 mol/mol). Two different sources of silica were used: silica fume (particle size  
 350 range of 100–1000 nm) and nano-silica (particle size range of 5–20 nm). Our  
 351 analysis of experimental data lead to the following conclusions.

- 352 1. The reaction yields C-S-H as the sole product, although portlandite and  
 353 unreacted silica may also be present in the final composition.
- 354 2. The Raman spectra confirm the XRD and TGA evidence that there is  
 355 only slight carbonation in the samples.
- 356 3. The Raman spectra reveal systematic changes with composition, notably  
 357 a broadening of the Si-O-Si symmetric bending at  $\sim 666 \text{ cm}^{-1}$  in the NS  
 358 samples with increasing C/S.
- 359 4. Isothermal calorimetry allows the rate of reaction at 25 °C to be monitored  
 360 over first 200 h, and indicates a strong dependence of the reaction rate on  
 361 the particle size.
- 362 5. Calorimetric data show that the overall kinetics is well described by a  
 363 simple exponential model. This allows the timescale for the completion of  
 364 the reaction to be estimated.
- 365 6. Heat flow rate data show the existence of a weak minimum and maximum

366 in the rate of reaction at 20–30 h after mixing. This feature is similar to  
 367 the well known induction period in the hydration tricalcium silicate C<sub>3</sub>S,  
 368 although the latter is more pronounced. Heat flow rate data around the  
 369 rate maximum can be described by a site-saturation Avrami model, with  
 370  $m \sim 1.5$ . The rate maximum is unexpected and deserves further study.

371 7. Mass balance calculations using TG and XRD composition data provide  
 372 estimates of the C/S ratio of the C-S-H formed, although in the absence  
 373 of any direct information on possible unreacted silica, these C/S ratios are  
 374 nominal lower limits. Nonetheless, there is strong indication that the C/S  
 375 of the C-S-H product increases as the C/S of the initial mix increases.

376 **Acknowledgement**

377 This work is supported by UK Engineering and Physical Sciences Research  
 378 Council, (EPSRC Grant No. EP/L014041/1 - DISTINCTIVE Consortium -  
 379 Decommissioning, Immobilisation and Storage soluTIons for NuClear wasTe In-  
 380 VEntories). The authors acknowledge the loan of an Raman InVia Spectrometer  
 381 from the EPSRC Engineering Instrument Pool. Data associated with research  
 382 published in this paper is accessible at: <http://dx.doi.org/10.15129/9a6e8793-f62f-4e0e-8c97-14d4ba104f71>.

384

385 **References**

386 **References**

- 387 [1] R. Yu, P. Spiesz, H. Brouwers, Effect of nano-silica on the hydration and  
 388 microstructure development of Ultra-High Performance Concrete (UHPC)  
 389 with a low binder amount, Construction and Building Materials 65 (2014)  
 390 140–150. doi:10.1016/j.conbuildmat.2014.04.063.
- 391 [2] Y. Qing, Z. Zenan, K. Deyu, C. Rongshen, Influence of nano-SiO<sub>2</sub> ad-  
 392 dition on properties of hardened cement paste as compared with sil-

- 393       ica fume, Construction and Building Materials 21 (3) (2007) 539–545.  
 394       doi:10.1016/j.conbuildmat.2005.09.001.
- 395       [3] G. Quercia, G. Hüsken, H. J. H. Brouwers, Water demand of amorphous  
 396       nano silica and its impact on the workability of cement paste, Cement and  
 397       Concrete Research 42 (2) (2012) 344–357. doi:10.1016/j.cemconres.  
 398       2011.10.008.
- 399       [4] H. Biricik, N. Sarier, Comparative study of the characteristics of nano  
 400       silica-, silica fume- and fly ash-incorporated cement mortars, Materi-  
 401       als Research 17 (3) (2014) 570–582. doi:[http://dx.doi.org/10.1590/  
 402       S1516-14392014005000054](http://dx.doi.org/10.1590/S1516-14392014005000054).
- 403       [5] S. Dittrich, J. Neubauer, F. Goetz-Neunhoeffer, The influence of fly ash  
 404       on the hydration of OPC within the first 44h- A quantitative in situ XRD  
 405       and heat flow calorimetry study, Cement and Concrete Research 56 (2014)  
 406       129–138. doi:10.1016/j.cemconres.2013.11.013.
- 407       [6] A. Kar, I. Ray, A. Unnikrishnan, J. F. Davalos, Microanalysis and  
 408       optimization-based estimation of C-S-H contents of cementitious systems  
 409       containing fly ash and silica fume, Cement and Concrete Composites 34 (3)  
 410       (2012) 419–429. doi:10.1016/j.cemconcomp.2011.09.008.
- 411       [7] R. F. Feldman, G. G. Carette, V. M. Malhotra, Studies on mechanics of  
 412       development of physical and mechanical properties of high-volume fly ash-  
 413       cement pastes, Cement and Concrete Composites 12 (4) (1990) 245–251.  
 414       doi:10.1016/0958-9465(90)90003-G.
- 415       [8] A. Lazaro, G. Quercia, H. J. H. Brouwers, J. W. Geus, Synthesis of a Green  
 416       Nano-Silica Material Using Beneficiated Waste Dunites and Its Application  
 417       in Concrete, World Journal of Nano Science and Engineering 03 (03) (2013)  
 418       41–51. doi:10.4236/wjnse.2013.33006.
- 419       [9] Y. Xu, D. Chung, Cement of high specific heat and high thermal con-  
 420       ductivity, obtained by using silane and silica fume as admixtures, Ce-

- 421       ment and Concrete Research 30 (7) (2000) 1175–1178. doi:10.1016/  
 422       S0008-8846(00)00296-9.
- 423       [10] H.-W. Song, S.-W. Pack, S.-H. Nam, J.-C. Jang, V. Saraswathy, Estima-  
 424       tion of the permeability of silica fume cement concrete, Construction and  
 425       Building Materials 24 (3) (2010) 315–321. doi:10.1016/j.conbuildmat.  
 426       2009.08.033.
- 427       [11] Y. Wei, W. Yao, X. Xing, M. Wu, Quantitative evaluation of hydrated  
 428       cement modified by silica fume using QXRD, 27Al MAS NMR, TG-DSC  
 429       and selective dissolution techniques, Construction and Building Materials  
 430       36 (2012) 925–932. doi:10.1016/j.conbuildmat.2012.06.075.
- 431       [12] G. Land, D. Stephan, The influence of nano-silica on the hydration of  
 432       ordinary Portland cement, Journal of Materials Science 47 (2) (2012) 1011–  
 433       1017. doi:10.1007/s10853-011-5881-1.
- 434       [13] L. Wang, D. Zheng, S. Zhang, H. Cui, D. Li, Effect of Nano-SiO<sub>2</sub> on the  
 435       Hydration and Microstructure of Portland Cement, Nanomaterials 6 (12)  
 436       (2016) 241. doi:10.3390/nano6120241.
- 437       [14] M. Kumar, S. K. Singh, N. Singh, Heat evolution during the hydration of  
 438       Portland cement in the presence of fly ash, calcium hydroxide and super  
 439       plasticizer, Thermochimica Acta 548 (2012) 27–32. doi:10.1016/j.tca.  
 440       2012.08.028.
- 441       [15] B. W. Langan, K. Weng, M. A. Ward, Effect of silica fume and fly  
 442       ash on heat of hydration of Portland cement, Cement and Concrete Re-  
 443       search 32 (7) (2002) 1045–1051. arXiv:arXiv:1011.1669v3, doi:10.  
 444       1016/S0008-8846(02)00742-1.
- 445       [16] M. Oltulu, R. ahin, Pore structure analysis of hardened cement mortars  
 446       containing silica fume and different nano-powders, Construction and Build-  
 447       ing Materials 53 (2014) 658–664. doi:10.1016/j.conbuildmat.2013.11.  
 448       105.

- 449 [17] J. Rossen, B. Lothenbach, K. Scrivener, Composition of CSH in pastes with  
 450 increasing levels of silica fume addition, *Cement and Concrete Research* 75  
 451 (2015) 14–22. doi:[10.1016/j.cemconres.2015.04.016](https://doi.org/10.1016/j.cemconres.2015.04.016).
- 452 [18] J. J. Thomas, J. J. Biernacki, J. W. Bullard, S. Bishnoi, J. S. Dolado,  
 453 G. W. Scherer, A. Luttge, Modeling and simulation of cement hydration  
 454 kinetics and microstructure development, *Cement and Concrete Research*  
 455 41 (12) (2011) 1257–1278. doi:[10.1016/j.cemconres.2010.10.004](https://doi.org/10.1016/j.cemconres.2010.10.004).
- 456 [19] Q. Zeng, K. Li, T. Fen-chong, P. Dangla, Determination of cement hy-  
 457 dration and pozzolanic reaction extents for fly-ash cement pastes, *Con-  
 458 struction and Building Materials* 27 (1) (2012) 560–569. doi:[10.1016/j.conbuildmat.2011.07.007](https://doi.org/10.1016/j.conbuildmat.2011.07.007).
- 460 [20] H. Taylor, Cement chemistry, 2nd Edition, Vol. 20, 1998. doi:[10.1016/S0958-9465\(98\)00023-7](https://doi.org/10.1016/S0958-9465(98)00023-7).
- 462 [21] I. Richardson, Tobermorite/jennite- and tobermorite/calcium hydroxide-  
 463 based models for the structure of C-S-H: applicability to hardened pastes  
 464 of tricalcium silicate,  $\beta$ -dicalcium silicate, Portland cement, and blends of  
 465 Portland cement with blast-furnace slag, metakaol, *Cement and Concrete  
 466 Research* 34 (9) (2004) 1733–1777. doi:[10.1016/j.cemconres.2004.05.034](https://doi.org/10.1016/j.cemconres.2004.05.034).
- 468 [22] I. Richardson, L. Black, J. Skibsted, R. Kirkpatrick, Characterisation of  
 469 cement hydrate phases by TEM, NMR and Raman spectroscopy, *Advances  
 470 in Cement Research* 22 (4) (2010) 233–248. doi:[10.1680/adcr.2010.22.4.233](https://doi.org/10.1680/adcr.2010.22.4.233).
- 472 [23] X. Cong, R. Kirkpatrick,  $^{29}\text{Si}$  MAS NMR study of the structure of calcium  
 473 silicate hydrate, *Advanced Cement Based Materials* 3 (3-4) (1996) 144–156.  
 474 doi:[10.1016/S1065-7355\(96\)90046-2](https://doi.org/10.1016/S1065-7355(96)90046-2).
- 475 [24] O. Mendoza, C. Giraldo, S. S. Camargo, J. I. Tobón, Structural and nano-  
 476 mechanical properties of Calcium Silicate Hydrate (C-S-H) formed from

- 477 alite hydration in the presence of sodium and potassium hydroxide, Ce-  
478 ment and Concrete Research 74 (2015) 88–94. doi:10.1016/j.cemconres.  
479 2015.04.006.
- 480 [25] S. Nath, S. Maitra, S. Mukherjee, S. Kumar, Microstructural and mor-  
481 phological evolution of fly ash based geopolymers, Construction and Build-  
482 ing Materials 111 (2016) 758–765. doi:10.1016/j.conbuildmat.2016.  
483 02.106.
- 484 [26] K. Garbev, M. Bornefeld, G. Beuchle, P. Stemmermann, Cell Dimensions  
485 and Composition of Nanocrystalline Calcium Silicate Hydrate Solid Solu-  
486 tions. Part 2: X-Ray and Thermogravimetry Study, Journal of the Ameri-  
487 can Ceramic Society 91 (9) (2008) 3015–3023. doi:10.1111/j.1551-2916.  
488 2008.02601.x.
- 489 [27] S. Grangeon, F. Claret, C. Lerouge, F. Warmont, T. Sato, S. Anraku,  
490 C. Numako, Y. Linard, B. Lanson, On the nature of structural disorder  
491 in calcium silicate hydrates with a calcium/silicon ratio similar to tober-  
492 morite, Cement and Concrete Research 52 (2013) 31–37. doi:10.1016/j.  
493 cemconres.2013.05.007.
- 494 [28] E. Tajuelo, K. Garbev, D. Merz, L. Black, I. G. Richardson, Thermal  
495 stability of C-S-H phases and applicability of Richardson and Groves' and  
496 Richardson C-(A)-S-H (I) models to synthetic C-S-H, Cement and Concrete  
497 Research 93 (2017) 45–56. doi:10.1016/j.cemconres.2016.12.005.
- 498 [29] I. G. Richardson, Model structures for C-(A)-S-H(I), Acta Crystallograph-  
499 ica Section B: Structural Science, Crystal Engineering and Materials 70 (6)  
500 (2014) 903–923. doi:10.1107/S2052520614021982.
- 501 [30] L. Black, C. Breen, J. Yarwood, K. Garbev, P. Stemmermann,  
502 B. Gasharova, Structural Features of C-S-H(I) and its Carbonation in Air:  
503 A Raman Spectroscopic Study. Part II: Carbonated Phases, Journal of  
504 the American Ceramic Society 90 (3) (2007) 908–917. doi:10.1111/j.  
505 1551-2916.2006.01429.x.

- 506 [31] K. Garbev, P. Stemmermann, L. Black, C. Breen, J. Yarwood,  
507 B. Gasharova, Structural features of C-S-H(I) and its carbonation in air-A  
508 Raman spectroscopic study. Part I: Fresh phases, Journal of the American  
509 Ceramic Society 90 (3) (2007) 900–907. doi:10.1111/j.1551-2916.2006.  
510 01428.x.
- 511 [32] P. W. Brown, J. Pommersheim, G. Frohndorff, A kinetic model for the  
512 hydration of tricalcium silicate, Cement and Concrete Research 15 (1)  
513 (1985) 35–41.
- 514 [33] J. J. Thomas, A new approach to modeling the nucleation and growth kinet-  
515 ics of tricalcium silicate hydration, Journal of the American Ceramic Soci-  
516 ety 90 (10) (2007) 3282–3288. doi:10.1111/j.1551-2916.2007.01858.x.
- 517 [34] J. W. Bullard, G. W. Scherer, J. J. Thomas, Time dependent driving forces  
518 and the kinetics of tricalcium silicate hydration, Cement and Concrete  
519 Research 74 (2015) 26–34. doi:10.1016/j.cemconres.2015.03.016.  
520 URL [http://www.sciencedirect.com/science/article/pii/  
521 S0008884615001027](http://www.sciencedirect.com/science/article/pii/S0008884615001027)
- 522 [35] S. Vyazovkin, C. Wright, Kinetics in solids, Annual Review of Physical  
523 Chemistry 48 (1) (1997) 125–149. doi:10.1146/annurev.physchem.48.  
524 1.125.
- 525 [36] Q. Lin, Z. Xu, X. Lan, Y. Ni, C. Lu, The reactivity of nano silica with cal-  
526 cium hydroxide, Journal of Biomedical Materials Research - Part B Applied  
527 Biomaterials 99 B (May) (2011) 239–246. doi:10.1002/jbm.b.31891.
- 528 [37] B. Lothenbach, P. Durdzinski, K. de Weerdt, Thermogravimetric analysis,  
529 in: A Practical Guide to Microstructural Analysis of Cementitious Materi-  
530 als, CRC Press–Taylor & Francis, 2015, Ch. 5, pp. 177–211.
- 531 [38] K. Garbev, M. Bornefeld, G. Beuchle, P. Stemmermann, Cell dimensions  
532 and composition of nanocrystalline calcium silicate hydrate solid solutions.

- 533 Part 1: Synchotron-based X-Ray Diffraction, Journal of the American Ce-  
534 ramic Society 91 (9) (2008) 3005–3014. doi:10.1111/j.1551-2916.2008.  
535 02601.x.
- 536 [39] A. Kumar, B. J. Walder, A. Kunhi Mohamed, A. Hofstetter, B. Srinivasan,  
537 A. J. Rossini, K. Scrivener, L. Emsley, P. Bowen, The Atomic-Level Struc-  
538 ture of Cementitious Calcium Silicate Hydrate, Journal of Physical Chem-  
539 istry C 121 (32) (2017) 17188–17196. doi:10.1021/acs.jpcc.7b02439.
- 540 [40] M. Moukwa, S. Farrington, D. Youn, Determination of Ca(OH)<sub>2</sub> in hy-  
541 drated cement paste by differential scanning calorimetry, Thermochimica  
542 Acta 195 (1992) 231–237. doi:10.1016/0040-6031(92)80066-6.
- 543 [41] S. Kawashima, P. Hou, D. J. Corr, S. P. Shah, Modification of cement-  
544 based materials with nanoparticles, Cement and Concrete Composites 36  
545 (2013) 8–15. doi:10.1016/j.cemconcomp.2012.06.012.
- 546 [42] S. Bae, C. Meral, J.-e. Oh, J. Moon, M. Kunz, P. J. Monteiro, Characteriza-  
547 tion of morphology and hydration products of high-volume fly ash paste by  
548 monochromatic scanning x-ray micro-diffraction ( $\mu$ -SXRD), Cement and  
549 Concrete Research 59 (2014) 155–164. doi:10.1016/j.cemconres.2014.  
550 03.001.
- 551 [43] L. P. Singh, S. K. Bhattacharyya, S. P. Shah, G. Mishra, U. Sharma,  
552 Studies on early stage hydration of tricalcium silicate incorporating silica  
553 nanoparticles : Part II, Construction and Building Materials 102 (2016)  
554 943–949. doi:10.1016/j.conbuildmat.2015.05.084.
- 555 [44] A. Stumm, K. Garbev, G. Beuchle, L. Black, P. Stemmermann, R. Nüesch,  
556 Incorporation of zinc into calcium silicate hydrates, Part I: formation of C-  
557 S-H(I) with C/S=2/3 and its isochemical counterpart gyrolite, Cement and  
558 Concrete Research 35 (9) (2005) 1665–1675. doi:10.1016/j.cemconres.  
559 2004.11.007.

- 560 [45] E. Wieland, J. Tits, D. Kunz, R. Dähn, Strontium Uptake by Cementitious  
561 Materials, Environmental Science & Technology 42 (2) (2008) 403–409.  
562 doi:10.1021/es071227y.
- 563 [46] Z. Jing, F. Jin, N. Yamasaki, E. H. Ishida, Hydrothermal synthesis of a  
564 novel tobermorite-based porous material from municipal incineration bot-  
565 tom ash, Industrial and Engineering Chemistry Research 46 (8) (2007)  
566 2657–2660. doi:10.1021/ie070016z.
- 567 [47] W. Guan, F. Ji, Z. Fang, D. Fang, Y. Cheng, P. Yan, Q. Chen, Low hy-  
568 drothermal temperature synthesis of porous calcium silicate hydrate with  
569 enhanced reactivity SiO<sub>2</sub>, Ceramics International 40 (3) (2014) 4415–4420.  
570 doi:10.1016/j.ceramint.2013.08.113.
- 571 [48] W. Sha, G. Pereira, Differential scanning calorimetry study of ordinary  
572 Portland cement paste containing metakaolin and theoretical approach of  
573 metakaolin activity, Cement and Concrete Composites 23 (6) (2001) 455–  
574 461. doi:10.1016/S0958-9465(00)00090-1.
- 575 [49] D. S. Klimesch, A. Ray, J.-P. Guerbois, Differential scanning calorime-  
576 try evaluation of autoclaved cement based building materials made with  
577 construction and demolition waste, Thermochimica Acta 389 (1-2) (2002)  
578 195–198. doi:10.1016/S0040-6031(02)00058-8.